arXiv:2002.11786v1 [cond-mat.mes-hall] 26 Feb 2020

Hematite at its thinnest limit

C. Bacaksiz, M. Yagmurcukardes, F. M. Peeters, and M. V. Milošević*
Theory of Functional Materials, Department of Physics,
University of Antwerp, Groenenborgerlaan 171, B-2020 Antwerp, Belgium and
NANOlab Center of Excellence, University of Antwerp, Belgium

Motivated by the recent synthesis of two-dimensional α-Fe_2O_3 [Balan *et al.* Nat. Nanotech. **13**, 602 (2018)], we analyze the structural, vibrational, electronic and magnetic properties of single- and few-layer α-Fe_2O_3 compared to bulk, by *ab-initio* and Monte-Carlo simulations. We reveal how monolayer α-Fe_2O_3 (hematene) can be distinguished from the few-layer structures, and how they all differ from bulk through observable Raman spectra. The optical spectra exhibit gradual shift of the prominent peak to higher energy, as well as additional features at lower energy when α-Fe_2O_3 is thinned down to a monolayer. Both optical and electronic properties have strong spin asymmetry, meaning that lower-energy optical and electronic activities are allowed for the single-spin state. Finally, our considerations of magnetic properties reveal that 2D hematite has anti-ferromagnetic ground state for all thicknesses, but the critical temperature for Morin transition increases with decreasing sample thickness. On all accounts, the link to available experimental data is made, and further measurements are prompted.

I. INTRODUCTION

Following the successful isolation of graphene,[1,2] an immense effort has been exerted on the synthesis of other two dimensional (2D) layered materials such as group III-V binary compounds (h-BN, h-AlN)[3–7] and transition-metal dichalcogenides (TMDs).[8–15] Most of these 2D materials have bulk counterparts that are formed by van der Waals (vdW) stacked layers. Beside those, the atomically thin layers of silicene[16,17] and germanene,[16] which have non-layered bulk forms, have been successfully synthesized. Over the last years, the synthesis of ultra-thin materials from their non-layered bulk counterparts has also attracted interest in the material science,[18–20] where one of the most recent successes is the extraction of ultra-thin α-Fe_2O_3 (2D hematite).[21]

Iron oxide is a well-studied material family including several structural phases. The family exhibits various electronic and magnetic properties, such as band gap ranging from insulator to semiconductor,[22–26] superparamagnetism,[27] and weak ferromagnetism.[28,29,31–34] Iron oxide has four different crystalline phases at ambient pressures: α-Fe_2O_3 (hematite), β-Fe_2O_3, γ-Fe_2O_3 (maghemite), and ε-Fe_2O_3. Among these phases, hematite is a thermodynamically stable polymorph of Fe_2O_3, and a well-known ferromagnet that undergoes magnetic phase transitions from paramagnetic to weak-ferromagnetic state at the Neel temperature (T_N) of 961 K, and from weak-ferromagnetic to anti-ferromagnetic state at Morin transition temperature (T_M) of 265 K.[28,29] In addition, it has optimal band gap for light absorption applications,[30] and has been widely investigated for several other technological applications such as gas sensing,[25,35] lithium-ion batteries,[36–38] water treatment,[39–41] and catalysis.[42]

It is already well established that nano-structuring of a material can significantly influence its magnetic and other properties due to quantum confinement and surface effects.[43] Such effects on α-Fe_2O_3 were also studied. Schroeer *et al.* reported that T_M of microcrystal hematite is depressed under negative pressure induced due to the lattice spacing.[45] Zysler *et al.* demonstrated that T_M increases as the size of hematite nanoparticles increases.[44] In addition, Sorescu *et al.* studied the weak ferromagnetic phase above T_M and an anti-ferromagnetic phase below T_M for different sizes and morphologies of hematite nanoparticles.[46] Only recently, the focus of research shifted to the effects of thickness, after Balan *et al.* synthesized atomically-thin hematite and reported that it exhibits optical band gap comparable with the bulk sample, and weak ferromagnetism at low temperature regime without any Morin transition.[21] In their report, two different 2D hematite samples were considered, exfoliated from [001] and [010] crystallographic directions, and [001] 2D samples were claimed to be more stable based on the molecular dynamics simulations. They also attempted to support the experimental results by a DFT study, however, they considered only on a monolayer structure, which was not present in experiment at all. In the meantime, 2D α-Fe_2O_3 (named hematene) was reported in experimental and in DFT-based study as a stable anti-ferromagnetic semiconductor,[47,48] same as bulk, which further clouds the conclusions regarding thickness dependence of the magnetic properties of hematite in its thinnest limit.

Motivated by above issues, and recognizing the importance of hematene as a newest member of the family of magnetic 2D materials (rapidly emerging after the synthesis of the first magnetic single-layer of CrI_3)[49] that may have many other uses as well, we here thoroughly investigate its thickness-dependent physical properties, namely structural, vibrational, electronic, and magnetic properties of monolayer, few-layer, and bulk α-Fe_2O_3 by performing density functional theory-based calculations and Monte-Carlo simulations. In doing so, we reveal how the atomistic thickness of α-Fe_2O_3 is clearly reflected in the Raman and visible range optical spectra, and the critical temperature, all relevant to the ongoing experi-

mental efforts in the field.

The paper is organized as follows. Details of the computational methodology are presented in Sec. II. The thickness-dependent structural, vibrational, electronic, optical, and magnetic properties of hematene versus few-layer and bulk hematite are then comparatively discussed in Secs. III A-III E. We summarize our results and conclusions in Sec. IV.

II. COMPUTATIONAL METHODOLOGY

To investigate the structural, vibrational, magnetic, and electronic, properties of a two-dimensional α-Fe_2O_3 crystal, first-principle calculations were performed in the framework of density functional theory (DFT) as implemented in the Vienna *ab-initio* simulation package (VASP).[50,51] The Perdew-Burke-Ernzerhof (PBE)[52] form of the generalized gradient approximation (GGA) was adopted to describe electron exchange and correlation. The Hubbard U term was included to be 4 eV for Fe atom in all calculations to account for the strong on-site Coulomb interaction.[54] The van der Waals (vdW) correction to the GGA functional was included by using the DFT-D2 method of Grimme.[53] The charge transfer in the system was determined by the Bader technique.[55]

The kinetic energy cut-off for plane-wave expansion was set to 600 eV and the energy was minimized until its variation in the following steps became lower than 10^{-6} eV. The Gaussian smearing method was employed for the total energy calculations. In order to capture the correct occupancy of the surface states, the width of smearing was set to 0.01 eV (checked to be sufficiently small for few-layer Fe_2O_3 samples). Total Hellmann-Feynman forces was taken to be 10^{-5} eV/Å for the structural optimization. $24 \times 24 \times 1$ Γ-centered k-point sampling was used in the primitive unit cells. To avoid interaction between successive layers in the out-of-plane direction, we used a vacuum spacing of 12 Å. Regarding the dielectric function calculations, $48 \times 48 \times 1$ Γ-centered k-point sampling was used and direct ($q = 0$) single-particle excitations from valence to conduction band were calculated. The local field effects were included at DFT level.

In order to investigate the dynamical stability of a monolayer hematene structure, the phonon band dispersions were calculated by the small displacement method, as implemented in the PHON code.[56] In addition, the first order off-resonant Raman activities of the phonon modes at the Γ point were obtained by calculating the change in the macroscopic dielectric tensor with respect to the normal mode describing each vibrational mode using finite-difference method.[57] A detailed theory of the Raman scattering can be found in our recent studies.[58,59]

To investigate the magnetic exchange parameters between the magnetic sites, we used four-state methodology,[60] which relies on mapping of the energetics of different magnetic configurations onto Heisenberg spin Hamiltonian:

$$H = \sum_{\langle ij \rangle_n} -J_n^{ij} S_i \cdot S_j, \tag{1}$$

where J_n^{ij} is the magnetic exchange parameter between ith and jth magnetic sites, indexed by n in the nearest-neighbor sequence. Considering two atomic sites, 1 and 2, which are the nearest neighbors of each other and the corresponding exchange parameter, J_1^{12}, the energy can be written as:

$$E = J_1^{12} S_1 \cdot S_2 + S_1 \cdot \mathrm{K}_1 + S_2 \cdot \mathrm{K}_2 + E_{others}. \tag{2}$$

Here the first term describes the interaction between sites 1 and 2, $\mathrm{K}_1 = \sum_{\langle 1j \neq 1,2 \rangle_n} J_n^{1j} S_1$ and $\mathrm{K}_2 = \sum_{\langle 2j \neq 1,2 \rangle_n} J_n^{2j} S_2$ are the interactions of site 1 with others and site 2 with others, respectively. Last term stands for the interaction between the sites different from 1 and 2. To isolate J_1^{12}, four different magnetic configurations were chosen as (i) $S_1 = S, S_2 = S$; (ii) $S_1 = -S, S_2 = S$; (iii) $S_1 = S, S_2 = -S$; (iv) $S_1 = -S, S_2 = -S$, and $S_{other} = S$, so that

$$\begin{aligned}
E^{(\mathrm{i})} &= E_{others} + J_1^{12} S^2 + S^2 K_1 + S^2 K_2, \\
E^{(\mathrm{ii})} &= E_{others} - J_1^{12} S^2 - S^2 K_1 + S^2 K_2, \\
E^{(\mathrm{iii})} &= E_{others} - J_1^{12} S^2 + S^2 K_1 - S^2 K_2, \\
E^{(\mathrm{iv})} &= E_{others} + J_1^{12} S^2 - S^2 K_1 - S^2 K_2.
\end{aligned}$$

This set of equations yields J_1^{12} as

$$J_1^{12} = \frac{E^{(\mathrm{i})} + E^{(\mathrm{iv})} - E^{(\mathrm{ii})} - E^{(\mathrm{iii})}}{4S^2}, \tag{3}$$

which is a general formula for any considered pair of magnetic sites.

The temperature-dependent magnetization of the system was then estimated by performing standard Metropolis Monte-Carlo (MC) simulations on top of the DFT-calculated magnetic exchange parameters, J_n's. Regarding the MC simulations, $4 \times 4 \times 1$ lattice with periodic boundary conditions in the lateral directions (out-of-plane periodicity was considered for bulk) was constructed. Randomly generated spin configuration was cooled down from 2500 to 0 K, where at each temperature $2{\times}10^3$ spin-flips per site were executed to obtain thermal equilibrium.

III. RESULTS AND DISCUSSION

A. Thickness-dependent structural properties

The well-known bulk α-Fe_2O_3 structure belongs to $R\bar{3}2/c$ space group in which ABC stacked buckled hexagonal sublayers of Fe atoms have octahedral coordination with six O atoms as shown in Fig. 1(a). In-plane and out-of-plane lattice parameters are found to be $a = b = 5.08$

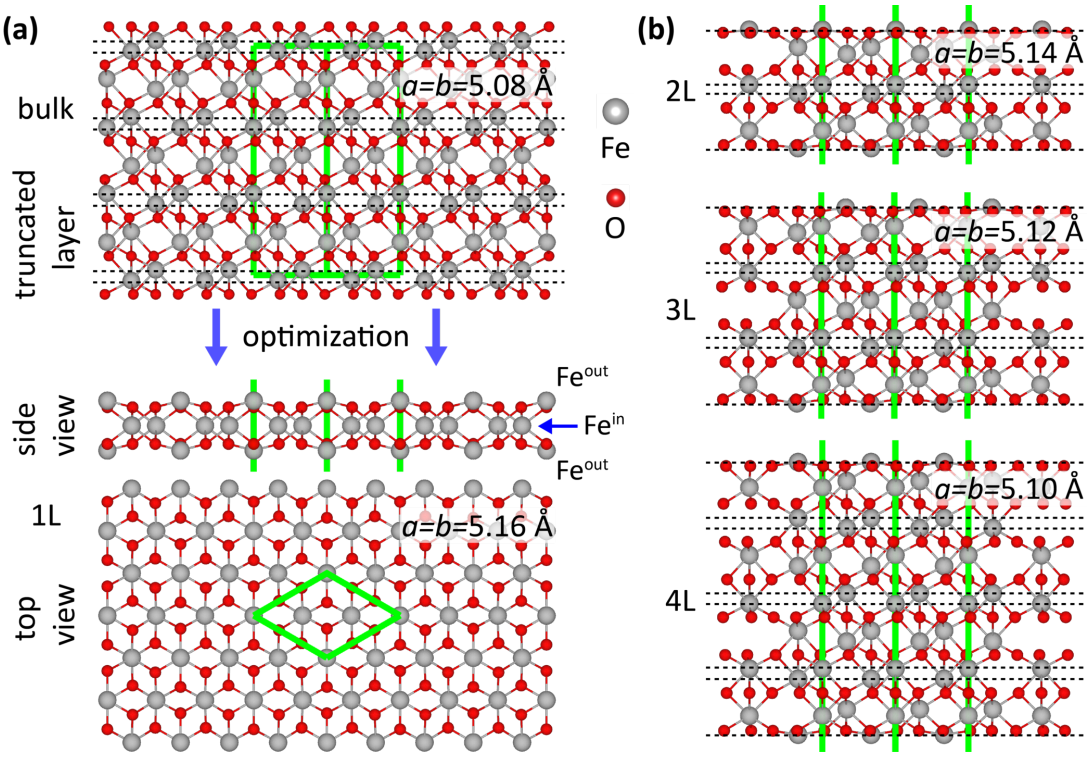


FIG. 1: (color online) (a) The side and top views of hematene truncated from the bulk α-Fe_2O_3 in the [001] direction, after optimization. Green line denotes the primitive unit cell. Two types of Fe atoms are also indicated as Fe^{in} and Fe^{out}. (b) The side view of the optimized structure of 2L, 3L, and 4L α-Fe_2O_3.

Åand $c = 13.72$ Å, as listed in Table I. Since Balan *et al.* reported that atomically thin layers exfoliated in [001] directions are more stable,[21] we consider the thickness-dependent properties for [001] hematite samples. As an initial structure, we truncated a layer from the bulk in the [001] direction, as shown by dashed lines in Fig. 1(a). The unit cell of the truncated layer consists of four Fe and six O atoms which fits the formula unit of Fe_2O_3. Differing from the bulk form, there are two types of Fe atoms due to the absence of the coexisting atoms in the out-of-plane direction: inner Fe atoms with the octahedral bond coordination, labeled Fe^{in}, and the outer Fe atoms with the trigonal pyramidal coordination, labeled Fe^{out} (see Fig. 1(a)).

TABLE I: In-plane lattice constants, a and b; out-of-plane lattice constant for bulk, c; the average distance between Fe^{out} atoms per number of layers, d; the electron donation per Fe atom, $\Delta\rho$, the first and second value discriminating Fe^{in} and Fe^{out}, respectively; the magnetic ground state, MS; the cohesive energy per unit formula, E_c; the energy band gap (GGA with $U = 4$ eV), E_{gap}.

	a (Å)	b (Å)	c (Å)	d (Å)	$\Delta\rho$ (e^-)	MS -	E_c (eV)	E_{gap} (eV)
Bulk	5.08	5.08	13.72	-	1.8	AFM	5.00	2.10
4L	5.10	5.10	-	4.12	1.8/1.6	AFM	4.90	M
3L	5.12	5.12	-	3.95	1.8/1.6	AFM	4.87	M
2L	5.14	5.14	-	3.60	1.8/1.6	AFM	4.81	M
1L	5.16	5.16	-	3.04	1.8/1.6	AFM	4.62	0.75

The optimized 1L structure (hematene), shown in Fig. 1(a), has a perfectly symmetric hexagonal sublattice of Fe^{in} atoms sandwiched by directly stacked two trigonal sublattices of Fe^{out} atoms. The octahedral coordination of Fe^{in} and trigonal pyramidal coordination of Fe^{out} atoms remain such. The space group of the new 2D structure is $P\bar{3}12/m$. As given in Table I, the lattice parameters are found to be $a = b = 5.16$ Å, slightly larger than those of bulk. The distance between the Fe^{out} atoms is $d = 3.04$ Å, smaller than 3.95 Åin bulk. It is also found that each Fe^{in} atom donates 1.8 e^- to an O atom. Fe^{out} donates 1.6 e^- which is slightly smaller due to having coordination 3 instead of 6.

Differing from the monolayer, the structural configurations and the bond coordination of the thicker systems, 2L, 3L, and 4L, remain similar to those of bulk α-Fe_2O_3, as shown in Fig. 1(b). Slight structural changes presented in Table I indicate that adjacent layer(s) in the out-of-plane direction prevent atoms from rearranging their position as obtained in the optimization of the 1L structure.

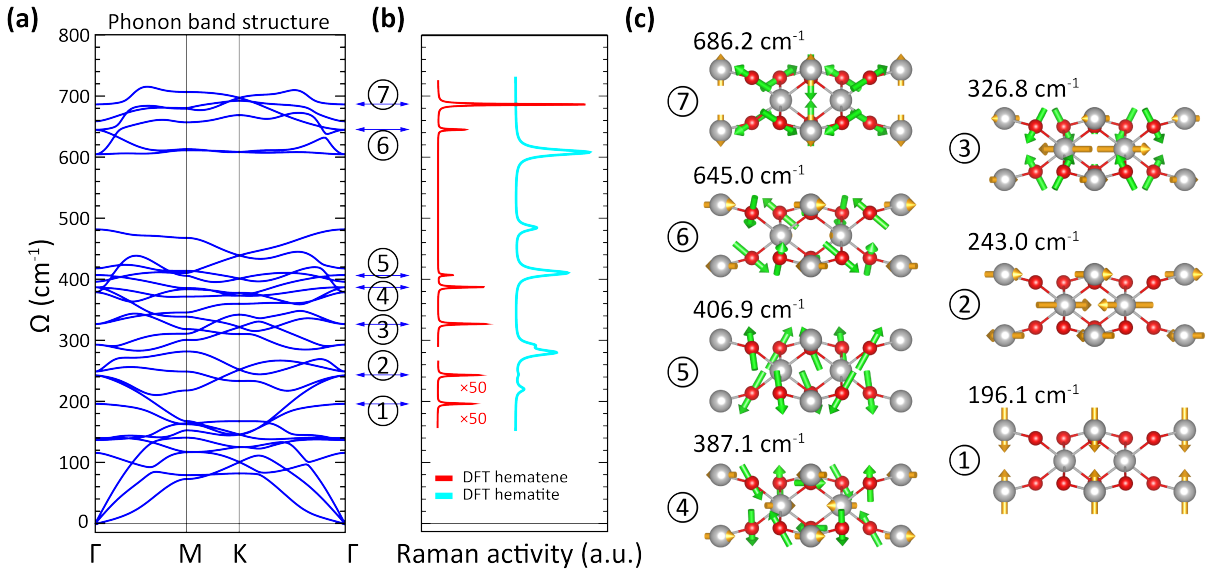


FIG. 2: (color online) (a) Phonon band structure of hematene through high symmetry points of the BZ. (b) Calculated Raman spectrum for hematene and bulk hematite (red and turquoise, respectively). (c) The vibrational characteristics of Raman active phonon modes of hematene.

B. Thickness-dependent vibrational properties

The dynamical stability of the optimized 1L α-Fe_2O_3 is examined by calculating its phonon band dispersion through the high symmetry points of the Brillouin zone (BZ), as shown in Fig. 2(a). It is evident that hematene is dynamically stable, and exhibits thirty phonon branches - three of which are acoustic. The highest frequency of the optical phonon branches at the Γ point is found to be 686.2 cm^{-1}, which is relatively large as compared to those of MX_2 where M=Mo, W, Re and X=S, Se (401.0−450.0 cm^{-1}).[58] Having optical phonon branches at higher frequency indicates the relatively high mechanical stiffness of 1L α-Fe_2O_3. For illustrative comparison, we also give the values of graphene (1555.0 cm^{-1}) and h-BN (1343.4 cm^{-1}).

For further elucidation of the vibrational properties, the first order off-resonant Raman activities of the phonon modes for 1L α-Fe_2O_3 are calculated and presented in Fig. 2(b). There are seven Raman active phonon modes which are assigned as 1-to-7 from low to high frequencies (see Fig. 2(c)). The seven Raman active modes can be categorized as three non-degenerate out-of-plane (having frequencies 196.1, 406.9, and 686.2 cm^{-1}) and four doubly-degenerate in-plane vibrational modes (with frequencies of 243.0, 326.8, 387.1, and 645.0 cm^{-1}). The mode at frequency 196.1 cm^{-1} has the lowest Raman activity and is attributed to the purely out-of-plane breathing-like vibration of Fe atoms (see Fig. 2(c)). Another non-degenerate phonon mode at the frequency of 406.9 cm^{-1} demonstrates the mostly out-of-plane vibration of O atoms while Fe atoms make no contribution. The highest frequency optical mode is found at 686.2 cm^{-1}, which is the most prominent peak and represents the purely out-of-plane vibration of Fe atoms and mostly in-plane vibration of O atoms. Notably, this phonon mode can only be observed in 2D α-Fe_2O_3 structures and is absent in bulk (or unobservable due to its negligibly small Raman activity). The doubly-degenerate phonon mode at 243.0 cm^{-1} has a low Raman activity and it is attributed to the in-plane vibration of Fe atoms against each other, while O atoms do not contribute to the vibration. The mode at 326.8 cm^{-1} arises from the in-plane opposite vibration of Fe atoms while O atoms vibrate in opposite out-of-plane directions at the top and the bottom of the layer. A similar vibrational character is found for the phonon mode at frequency 387.1 cm^{-1}, in which adjacent O atoms vibrate in opposite out-of-plane directions. Finally, the phonon mode at 645.0 cm^{-1} has similar vibrational character with the mode at frequency 387.1 cm^{-1}. In this mode, the Fe^{in} atoms have relatively small contribution to the vibration.

The calculated Raman spectrum of bulk α-Fe_2O_3 reveals also seven Raman active peaks. Two out-of-plane non-degenerate phonon modes are assigned as A_{1g} modes at the frequencies of 220.0 and 484.3 cm^{-1}. Other five Raman active modes having frequencies 244.0, 280.0, 292.1, 410.4, and 607.9 cm^{-1} are doubly-degenerate and are assigned as E_g modes.

In Fig. 3, we present our results on the Raman spectra of α-Fe_2O_3 structures from monolayer to bulk, with comparison to the experimental observations reported by Balan *et al.*.[21] Since the intensities of the peaks are relatively low at the frequencies below 350 cm^{-1}, we zoom in on the spectra in 150-350 cm^{-1} range in the left panel of the figure, where peak-intensities are multiplied by given factors to facilitate the observation of the frequency-shift. The dashed lines track the peak-positions with respect to

the experimental peak-positions on the frequency axis. In general, the calculated Raman spectrum of the bulk shows good agreement with the experiment of Ref.21. For the 2-4L samples, the calculated Raman spectra capture the main features of the experimental spectrum of a quasi-2D structure, with slightly stronger shift of the peak frequencies as compared to the experimental shift upon exfoliation. However, monolayer Fe_2O_3 exhibits distinctive peak positions. Balan *et al.* demonstrated in their thickness measurement the absence of samples as thin as a monolayer of either [001] (3.04 Å) or [010] (3.09 Å) phases; our results for Raman response of a monolayer corroborate that fact, as experimentally measured Raman spectrum is completely different from the Raman spectrum expected for a monolayer.

We start the discussion with the peaks in the range 150-350 cm^{-1}, zoomed out in the left panel of Fig. 3. The frequency of the A_g mode displays phonon hardening with increasing thickness. Its frequency in a monolayer (196.1 cm^{-1}) hardens to 211.5 cm^{-1} in 2L α-Fe_2O_3, and further to 212.7 and 214.3 cm^{-1} in 3L and 4L structures, respectively. Since this mode is attributed to the vibration of Fe^{out} atoms, the change in its frequency decreases with increasing thickness. Therefore, for sufficiently thick samples its frequency is very close to the bulk case. Notably, this behavior is rather different from a layered (vdW) material, because in a non-layered material, the

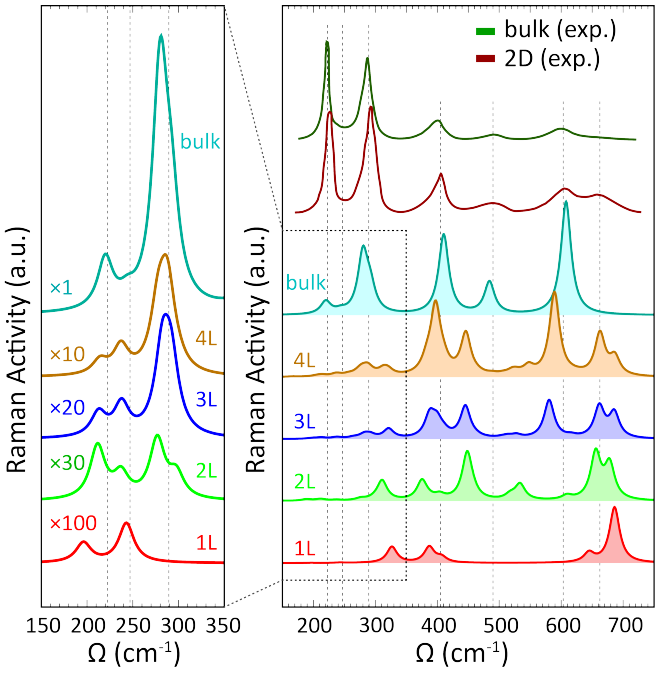


FIG. 3: (color line) Calculated Raman spectrum for 1L, 2L, 3L, 4L, and bulk. Above them, the experimental Raman spectrum for bulk and 2D α-Fe_2O_3 is shown, as reported in Ref.21. The left panel zooms in on the low-intensity peaks in the frequency range 150-350 cm^{-1}. The intensities are multiplied by a given factor to enhance the visibility of the peaks.

coordination, length, and strength of the bonds, also the surface reconstructions, may change significantly with thickness. As compared to the experiment,[21] our finding indicates that a very small frequency shift of A_g mode compared to bulk is a signature of a few-layer thick sample. Contrarily, the bulk out-of-plane mode at frequency 484.3 cm^{-1} displays phonon softening as the structure is thinned down to 2L. Its frequency is found to be 457.1, 463.5, and 465.4 cm^{-1} in 2L, 3L, and 4L structures, respectively. In the case of E_g modes, phonon hardening is mostly found with increasing thickness. The mode at frequency 276.7 cm^{-1} (in 2L structure) displays phonon hardening to 292.1 cm^{-1} (in bulk) and it is attributed to the in-plane shear vibration of the Fe atoms. Moreover, the phonon mode having frequency 533.6 cm^{-1} in 2L crystal hardens to 607.9 cm^{-1} in bulk crystal. Notably, those two E_g modes are entirely absent in the 1L case. On the other hand, two particularly Raman active phonon modes at high frequencies appear in 2D structures, while being absent in the bulk crystal. Those two modes are found to be attributed to the mixed in- and out-of-plane vibrations of O atoms while the Fe atoms vibrate in-plane or out-of-plane (modes 6 and 7 in Fig. 2(c)). The phonon mode at 645.0 cm^{-1} in 1L hardens to 655.7, 661.6, and 662.6 cm^{-1} in 2L, 3L, and 4L structures, respectively. It is clear that the increment of the phonon frequency decreases with layer thickness. However, the Raman activity of the phonon mode decreases as the structure becomes thicker, and disappears for bulk hematite. Notably, these two phonon modes exhibit distinctive features for distinguishing of 2D structures from bulk, since they predominantly arise from vibrations of surface atoms. It is rather remarkable that the phonon frequency differences between bulk and exfoliated samples reported by Balan *et al.* closely resemble those in our results down to 2L structure.[62] However, we also show that [001] monolayer hematene exhibits a completely distinctive Raman spectrum from the thicker structures, which may serve as a tool to distinguish true monolayer hematene from few-layer hematite in future experiments.

C. Thickness-dependent electronic properties

The calculated electronic band structure of 1L α-Fe_2O_3 is shown in Fig. 4(a). The band structure has asymmetric dispersion depending on the spin component. The blue curve (denoting *up*-spin, $S_\uparrow$), has its valence band maximum (VBM), which is also global maximum, at the K point. The $S_\uparrow$ component shows mid-gap states, dispersive over the energy axis between $0.75-0.94$ eV in all directions of the BZ, indicating that the mid-gap band is conductive with minimum at the Γ point. Therefore, the conduction band minimum (CBM) of the $S_\uparrow$ component is the global minimum and makes hematene an indirect band-gap semiconductor with a band gap of 0.75 eV. In addition, regardless of the mid-gap states, the conduc-

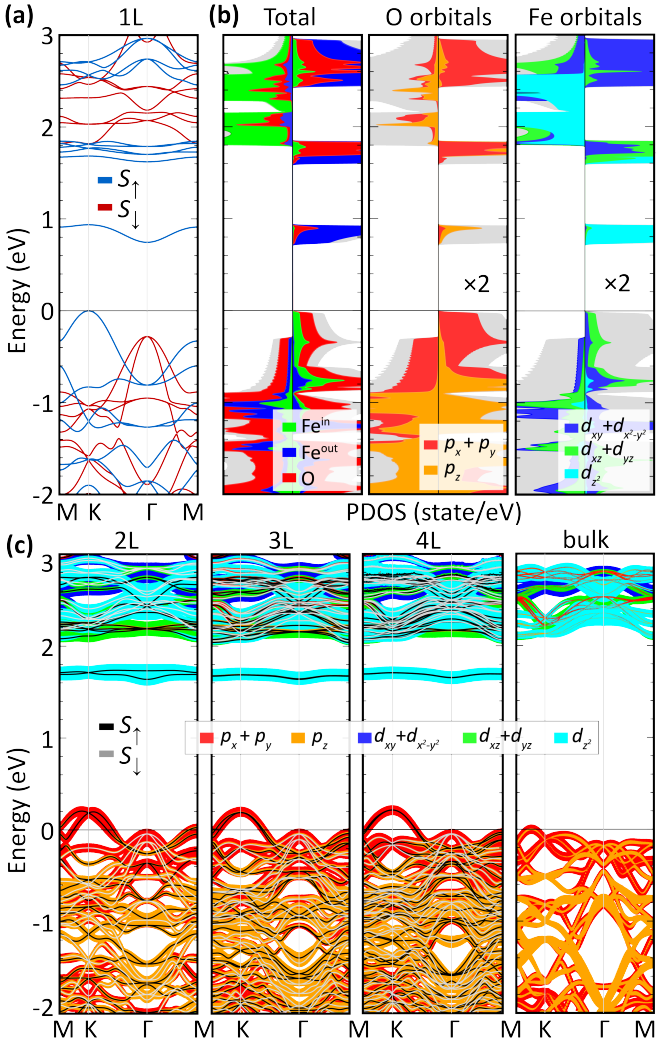


FIG. 4: (color line) (a) The spin-polarized electronic band structure of 1L α-Fe_2O_3. (b) Atom- (left) and orbital-decomposed partial density of states (pDOS) of 1L α-Fe_2O_3 , with color codes given in the graphs. The grey regions are the total density of state given as a reference for comparison. (c) Orbital-decomposed electronic band structure of 2L, 3L, 4L, and bulk α-Fe_2O_3.

tion band of the $S_\uparrow$ component has a minimum also at the K point with energy of 1.62 eV. Note that all extreme points including the mid-gap band originate from a single spin component of $S_\uparrow$.

On the other hand, the *down*-spin ($S_\downarrow$) component, with corresponding red lines in Fig. 4(a), possesses its valence band maximum with two degenerate light and heavy hole bands at the Γ point. The VBM of the $S_\downarrow$ component appears at the M point with an energy of -0.28 eV with respect to Fermi-level. The conduction band of the $S_\downarrow$ component at the M point is at 1.82 eV, giving rise to a band gap of $S_\downarrow$ component of 2.10 eV.

For further analysis of the electronic properties, the atom- and orbital-decomposed partial density of states (pDOS) of 1L α-Fe_2O_3 was calculated. In the left panel of Fig. 4(b), the atom-decomposed pDOS for Fe^{in}, Fe^{out}, and O atoms is shown. The VBM, in which only the $S_\uparrow$ states exist, is dominated by the oxygen states and considerable amount of states originate from only Fe^{in} atoms. For the $S_\downarrow$ part, most of the states are from oxygen, yet only the states of Fe^{out} atoms have contributions. The mid-gap band, on the other hand, is dominated by the Fe^{out} states and there is a small contribution from the oxygen states.

In central and right panels of Fig. 4(b), the pDOS for p-orbitals of O atoms and d-orbitals of Fe atoms are shown, respectively. It is revealed that the O domination of the VBM (central panel), originates from the p_x and p_y orbitals, while most of the Fe states (right panel) stem from in- and out-of-plane hybrid orbitals of d_{xz} and d_{yz}, with small contributions from d_{xy} and $d_{x^2-y^2}$ orbitals. The $S_\downarrow$ part of the valence band has a similar picture considering the O orbitals, however, the only contribution of Fe atoms are from d_{xy} and $d_{x^2-y^2}$ orbitals.

The mid-gap states, on the other hand, originate mostly from the d_{z^2} orbitals of Fe^{out} atoms, as shown in left and right panels of Fig. 4(b), which is a typical example of the conductive surface states with a single chanel. The higher energies of the CB consist of the combination of p-orbitals of O atoms and d-orbitals o Fe.

In order to describe the change of the electronic properties with thickness, we calculate the orbital-decomposed electronic band structures of 2-4L and bulk α-Fe_2O_3 shown in Fig. 4(c). It is clearly seen that all few-layer structures have bands crossing the Fermi level which makes them metallic. These bands are dominated by p_x and p_y orbitals of O atoms. Note that in order to obtain accurate occupancies of the states around the Fermi-level in a layer exfoliated from a non-van der Waals material, the smearing parameter should be carefully chosen. If the smearing parameter is inappropriately large, the dangling bonds can be occupied and the Fermi-level can be shifted into the band gap, leading to incorrect conclusions about the electronic properties of the sample.[63] Therefore, we decreased our smearing parameter down to 0.01 eV, which allowed us to capture the dangling bonds of O atoms in 2-4L samples.

Regarding the higher energy features of the band structures, all few-layer systems exhibit mid-gap bands, dominated mainly by d_{z^2} orbitals of Fe atoms, and the spin states are split. The bulk system, on the other hand, has degenerate spin states in the band structure. It is clear that the anisotropic spin channels, the mid-gap states and the states crossing the Fermi level in few-layer structures are a consequence of the surface.

D. Thickness-dependent optical properties

In order to investigate the optical properties, we calculated the dielectric function of bulk and 1-4L α-Fe_2O_3, by considering the direct excitation between the single-particle states. Then we compare the results with the

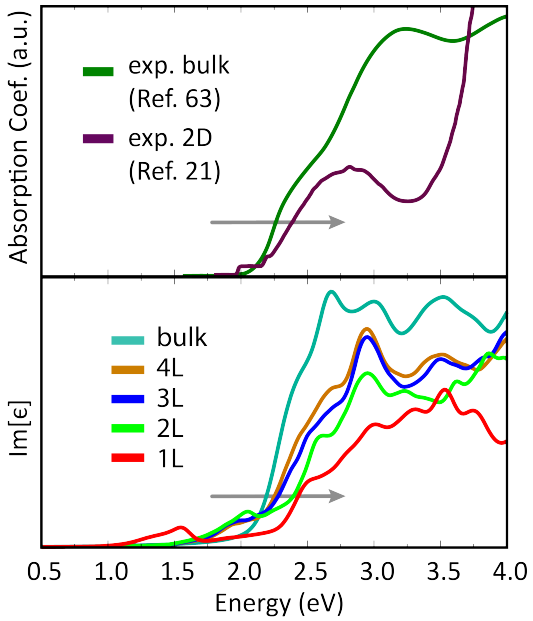


FIG. 5: (color online) Top panel: The experimentally-obtained absorption coefficients for bulk and 2D sample. Bottom panel: Calculated dielectric functions of 1L, 2L, 3L, 4L, and bulk. Arrow indicates the direction of change with thinning the sample.

experimental measurements on bulk[61] and 2D[21] samples, shown in Fig. 5. Note that the optical gaps taken from the measured and from the calculated optical spectra for a bulk system *perfectly match*, which yields confidence in the theoretical methodology to directly and reliably compare the calculated spectra of 1-4L systems with the experimentally obtained spectrum of a 2D sample.[21]

In general, the experimental spectra of bulk and 2D structure exhibit two main features. (i) When the structure thinned down from bulk to 2D, the prominent features shift to higher energy. That shift is also clearly seen in our calculated spectra. (ii) 2D spectrum exhibits a small step-like feature at the lower-energy edge of the prominent peak, while the bulk peak rises abruptly - which are also confirmed by the calculated spectra.

Looking deeper in the data, the calculated spectrum of hematene (red line) displays its lowest transition at ∼1.5 eV, which is only possible when the mid-gap states of 1L shown in Fig. 4 are optically active. From pDOS analysis, we infer that the peak at ∼1.5 eV stems mainly from the optical transitions between p_x-p_y states of oxygen atoms at ∼-0.4 eV, and d_{z^2} of Fe^{out} at ∼0.75−0.94, which correspond to mid-gap band. Recalling the results of the previous section, it is revealed here that those transitions are possible for the single-spin state. With its distinct mid-gap peak, the calculated spectrum for hematene does not match the experimentally seen absorption spectrum for 2D α-Fe_2O_3 in Ref.21, corroborating the fact that the 2D structure in experiment was thicker. As shown in our data, the thicker structures of 2-4L exhibit step-like feature at ∼1.9 eV, coinciding with the lower energy edge of the prominent peak. Similarly to mid-gap peak of 1L, those step-like features originate from the transitions between occupied p_x and p_y orbitals of oxygen and mid-gap d_{z^2} orbital of surface Fe atoms. Note that for 2-4L structures there are bands which are crossing the Fermi-level due to dangling bonds of O atoms which is shown in Fig. 4(c), however, there is no optical transition found from the occupied bands to those dangling states which are just above the Fermi-level. Therefore, 2-4L α-Fe_2O_3 has optical band gap, even though it has metallic features originating from optically inactive surface states.

This optical spectrum analysis therefore reveals the clear distinction between the spectra of few-layer and monolayer samples, and also between few-layer and bulk hematite. Our calculations also confirm that experimental realization of 2D α-Fe_2O_3 to date was in 2L and thicker forms, and not a monolayer.

E. Thickness-dependent magnetic properties

In this section, we discuss the thickness-dependent magnetic properties of 1-4L and bulk α-Fe_2O_3. We first investigate the ground-state magnetic states for all structures by comparing the energetics of the different possible magnetic configurations. Each Fe atom has the magnetic moment of $|m| = 4\ \mu_B$ in the ground state for all structures. It is found that bulk α-Fe_2O_3 has an antiferromagnetic (AFM) ground state shown in Fig. 6(a), which agrees with the earlier results in literature.[47,48] Basically, magnetization of Fe atoms in the hexagonal buckled sublayers are parallel. The sublayers have antiparallel magnetization with respect to each other. The same configuration is also found as the ground state for the 2-4L α-Fe_2O_3. The state for 1L is shown in Fig. 6(a) next to bulk, and is also resembling the state truncated from the bulk AFM state.

The energetics of different magnetic configurations also allows us to calculate the magnetic exchange parameters between the magnetic sites. We map the energetics to Heisenberg spin Hamiltonian given in Eq. (1) by applying the nearest-neighbor (NN) approximation following the procedure given in Sec. II. In the bulk structure, as depicted in Fig. 6(a), the magnetic sites are identical in terms of number of nth nearest neighbors and the corresponding bond length. However, for 1-4L structures, the number of nth nearest neighbors and the bond lengths differ depending on the position of the magnetic site in question in the out-of-plane direction. Therefore, we performed different sets of calculations for the magnetic exchange parameters experienced by an atom, depending on its position in the sample. The obtained values are listed in Table II.

In order to obtain the magnetic properties beyond the ground state, we performed MC simulations based on Ising model, using the determined exchange parameters, to predict the temperature-dependent magnetic

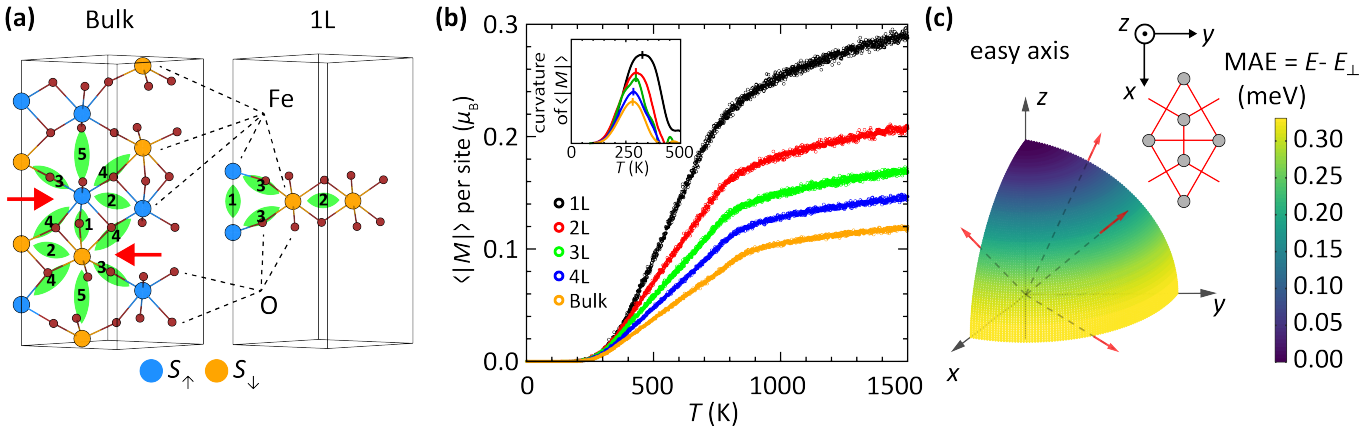


FIG. 6: (color line) (a) Schematic illustration of the magnetic exchange parameters between Fe atoms for bulk (left) and 1L (right). Shown numbers are the indices of the exchange coefficients J_n in Eq. (1). (b) The averaged absolute magnetization of 1-4L and bulk systems as a function of temperature. Inset shows T_c as a function of thickness, obtained as the temperature of the maximal curvature of the corresponding magnetization curve. (c) The magnetic anisotropy energies of monolayer hematene are projected on a spherical surface, at which normal vectors correspond to magnetization direction, as shown by the arbitrarily placed red arrows.

properties such as critical temperature (T_c). However, the Ising model considers only up/down collinear spins, hence yields much overestimated barriers for magnetic transitions. As a consequence, our trial MC calculation using DFT-obtained exchange parameters for the bulk system yield much larger T_c for ferromagnetic to anti-ferromagnetic transition as compared to reality. To accommodate this issue, we rescaled all exchange parameters by a constant factor (0.65) so that the theoretically obtained $T_c = 281$ K is close to the experimentally measured T_c of 265 K for bulk hematite.[28,29]

TABLE II: The magnetic exchange parameters for monolayer, few-layer, and bulk hematite, J_n, where n is the index of the considered nearest neighbor. For the 2-4L systems, J_n's vary depending on the pair position in the sample. We list them top to bottom as from outermost to innermost layer of sample. The last column gives the obtained critical temperature, T_c.

	J_1 (meV)	J_2 (meV)	J_3 (meV)	J_4 (meV)	J_5 (meV)	T_c (K)
Bulk	1.20	1.31	10.37	7.06	0.50	281
4L	0.58	1.64	16.72	10.26	-0.21	285
	1.05	1.09	10.13	7.83	0.64	
	1.02	1.45	8.56	6.91	0.56	
				7.01	0.51	
				6.89		
				5.81		
3L	0.47	1.63	16.51	10.15	-0.33	297
	0.92	1.09	8.29	10.03	0.52	
		1.35		6.89	0.45	
				6.63		
				5.69		
2L	0.37	1.73	16.44	9.79	-0.67	299
		0.83	8.05	7.32	0.43	
				5.57		
1L	0.94	2.13	11.88			326

For each structure, starting from 2500 K, the system is cooled down to 0 K, and the average absolute magnetic moment per magnetic site, $\langle |M| \rangle$, is obtained as a function of temperature, as shown in Fig. 6(b). From the point where the magnetization curve exhibits maximal curvature as a function of temperature, we determine the critical temperature (T_c) at which the system goes from weak ferromagnetic to the anti-ferromagnetic state, as listed in Table II. Of course, the behavior as a function of temperature is also very instructive, as will be discussed further on.

In general, as shown in Fig. 6(b), the magnetization curves exhibit similar behavior for all samples, with overall magnetization decrease with sample thickness. All curves exhibit a strong curvature in the range $700 - 860$ K where the anti-ferromagnetic exchange interaction starts to take over. For different samples, the anti-ferromagnetic states gain dominance at temperatures 270-350 K. It should be pointed out that our MC simulation cannot capture the Néel temperature (T_N) of 961 K[28] for bulk hematite, due to the Ising approximation in which all spin magnetic moments are considered collinear (causing also the high-temperature ferromagnetism as discussed previously).

We start the discussion from the bulk sample, where the magnetization (orange dots in Fig. 6(b)) gradually decreases from on-site average of $\sim$0.12 μ_B at 1500 K down to 0.10 μ_B at 854 K, where the anti-ferromagnetic state starts to build up. T_c is found to be 281 K and the magnetization at room temperature is found to be 0.004 μ_B, which is consistent with the experimentally

determined value of 0.005 μ_B.[29] The magnetization of 4L structure (blue dots in Fig. 6(b)) is slightly above the one of bulk. The antiferromagnetic interactions become apparent at ∼816 K and dominate below $T_c = 285$ K, which is nearly the same as for bulk. The magnetization for 3L sample exhibits the same behavior as 4L and bulk structures, with slightly higher magnetization. The influence of the anti-ferromagnetic exchange arises at ∼771 K. T_c is found to be 297 K, which can be considered as a significant jump as compared to bulk and 4L samples. The results for 2L system are also similar to thicker samples in terms of the form of the magnetization curve, with further increased magnetization compared to thicker samples. The anti-ferromagnetic exchange interaction is taking over at 790 K, and T_c is found to be 299 K.

The most significant changes are obtained when the sample is thinned down to a monolayer, even though the behavior of the magnetization curve still resembles the one found for thicker samples. The weak ferromagnetism is largest of all samples and the anti-ferromagnetic interaction rises at ∼711 K which is a significantly lower threshold temperature compared to 2L and 3L samples. The critical temperature of $T_c = 326$ K is above the room temperature and the highest of all considered sample thicknesses.

Our MC simulation therefore reveals that considering T_c values, bulk and 4L system on one side, and 2L and 3L systems on the other, are similar and can be considered equivalent. Monolayer hematene is different from thicker structures in all aspects, which is expected due to structural differences (cf. Fig. 1). Here it should be noted that our results do not support the findings of Ref.21, where FM to AFM transition was not observed for few-layer 2D α-Fe_2O_3 down to low temperature. In addition to that, we speculate that in the experiment AFM phase could be further suppressed by the substrate effects so the system can preserve ferromagnetic behavior at even lower temperature. We reiterate the fact that true monolayer hematene exhibits much higher T_c than 2-3L structures, so Morin transition should be experimentally observable there with lowered temperatures.

To complete the discussion, the magnetic anisotropy energies (MAE) of monolayer hematene were investigated as well. In Fig. 6(c), the MAE is projected on a sphere surface with respect to magnetization direction. There, x, y, and z directions correspond to *arm-chair*, *zig-zag*, and out-of-plane directions, respectively. The minimum energy direction is found to be parallel to the z, i.e. to the out-of-plane direction, and the corresponding energy is set to 0.0 meV. MAE is found to be 0.34 meV when the magnetization is parallel to the plane of the structure and does not change with the horizontal angle.

IV. CONCLUSIONS

In summary, motivated by the recent experimental synthesis of few-layer thick hematite, i.e. 2D α-Fe_2O_3,[21] we investigated theoretically the structural, vibrational, magnetic, and electronic properties of monolayer, few-layer and bulk α-Fe_2O_3. The monolayer α-Fe_2O_3, for which we reserved the name hematene, was shown to indeed be stable, although not yet seen experimentally. Our calculated Raman spectrum shows that hematene can be clearly distinguished from few-layer and thicker structures, since the frequency shifts (weak when thinning the sample) are found to be the largest between monolayer and two-layer samples. We also find that all 2D structures exhibit distinctive Raman active modes in high frequencies that are absent in bulk.

In the electronic band structure, hematene exhibits strong spin asymmetry. Valence-band maximum (VBM), mid-gap bands and conduction-band minimum all belong to one spin state. VBM is dominated by p_x and p_y orbitals of oxygen, while the mid-gap band originates mostly from the d_{z^2} orbital of surface iron atoms.

Our calculated optical spectra of monolayer, few-layer, and bulk structures show that the prominent part of the optical spectrum shifts to higher energy when the system is thinned down, as seen in experiment. 2-4 layer structures also exhibit a small step at the onset energy of the prominent peak, also seen in experiment, originating from the transition between the p_x and p_y of oxygen atoms to d_{z^2} of surface iron. The similar type of transition is responsible for the mid-gap peak of a monolayer structure, whose separation from the prominent peak is another feature to distinguish true hematene from few-layer samples.

Finally, our magnetic simulations based on DFT-determined magnetic exchange parameters and subsequent Monte-Carlo simulations show that all considered structures display transitions from weak ferromagnetic to anti-ferromagnetic state with decreasing temperature. We note however that monolayer hematene exhibits higher T_c in our calculations, hence there the transition to AFM state should be easier to detect experimentally.

Owing to its tunability with atomistic changes in thickness, magnetism in a broad temperature range (including room temperature), optical bandgap in the visible range, as well as the spin-dependent electronic and optical properties, 2D α-Fe_2O_3 puts itself forward as a candidate for diverse technological applications. Taking all our findings at face value, we conclude that 2D α-Fe_2O_3 is certainly worth of further investigation and use in functional heterostructures.

Acknowledgments

This work was supported by Research Foundation-Flanders (FWO-Vlaanderen). Computational resources

were provided by Flemish Supercomputer Center (VSC), and TUBITAK ULAKBIM, High Performance and Grid Computing Center (TR-Grid e-Infrastructure). Part of this work was also supported by FLAG-ERA project TRANS-2D-TMD and TOPBOF-UAntwerp. M. Y. was supported by a postdoctoral fellowship from the Flemish Science Foundation (FWO-Vl).

* Electronic address: milorad.milosevic@uantwerpen.be

[1] K. S. Novoselov, A. K. Geim, S. V. Morozov, D. Jiang, Y. Zhang, S. V. Dubonos, I. V. Grigorieva, and A. A. Firsov, Science **306**, 666 (2004).

[2] K. S. Novoselov, A. K. Geim, S. V. Morozov, D. Jiang, M. I. Katsnelson, I. V. Grigorieva, S. V. Dubonos, and A. A. Firsov, Nature **438**, 197 (2005).

[3] H. Sahin, S. Cahangirov, M. Topsakal, E. Bekaroglu, E. Akturk, R. T. Senger, and S. Ciraci, Phys. Rev. B **80**, 155453 (2009).

[4] Q. Wang, Q. Sun, P. Jena, and Y. Kawazoe, ACS Nano **3**, 621 (2009).

[5] K. K. Kim, A. Hsu, X. Jia, S. M. Kim, Y. Shi, M. Hofmann, D. Nezich, J. F. Rodriguez-Nieva, M. Dresselhaus, T. Palacios, and J. Kong, Nano Lett. **12** (1), 161 (2012).

[6] P. Tsipas, S. Kassavetis, D. Tsoutsou, E. Xenogiannopoulou, E. Golias, S. A. Giamini, C. Grazianetti, D. Chiappe, A. Molle, M. Fanciulli, and A. Dimoulas, Appl. Phys. Lett. **103**, 251605 (2013).

[7] C. Bacaksiz, H. Sahin, H. D. Ozaydin, S. Horzum, R. T. Senger, and F. M. Peeters, Phys. Rev. B **91**, 085430 (2015).

[8] R. A. Gordon, D. Yang, E. D. Crozier, D. T. Jiang, and R. F. Frindt, Phys. Rev. B **65**, 125407 (2002).

[9] J. N. Coleman, M. Lotya, A. O'Neill, S. D. Bergin, P. J. King, U. Khan, K. Young, A. Gaucher, S. De, R. J. Smith, I. V. Shvets, S. K. Arora, G. Stanton, H. Y. Kim, K. Lee, G. T. Kim, G. S. Duesberg, T. Hallam, J. J. Boland, J. J. Wang, J. F. Donegan, J. C. Grunlan, G. Moriarty, A. Shmeliov, R. J. Nicholls, J. M. Perkins, E. M. Grieveson, K. Theuwissen, D. W. McComb, P. D. Nellist, and V. Nicolosi, Science **331**, 568 (2011).

[10] Q. H. Wang, K. Kalantar-Zadeh, A. Kis, J. N. Coleman, and M. S. Strano, Nat. Nanotech. **7**, 699 (2012).

[11] J. S. Ross, P. Klement, A. M. Jones, N. J. Ghimire, J. Yan, D. G. Mandrus, T. Taniguchi, K. Watanabe, K. Kitamura, W. Yao, D. H. Cobden, and X. Xu, Nat. Nanotech. **9**, 268 (2014).

[12] H. Sahin, S. Tongay, S. Horzum, W. Fan, J. Zhou, J. Li, J. Wu, and F. M. Peeters, Phys. Rev. B **87**, 165409 (2013).

[13] S. Tongay, H. Sahin, C. Ko, A. Luce, W. Fan, K. Liu, J. Zhou, Y. S. Huang, C. H. Ho, J. Yan, D. F. Ogletree, S. Aloni, J. Ji, S. Li, J. Li, F. M. Peeters, and J. Wu, Nat. Comm. **5**, 3252 (2014).

[14] S. Horzum, D. Cakir, J. Suh, S. Tongay, Y. S. Huang, C. H. Ho, J. Wu, H. Sahin, and F. M. Peeters, Phys. Rev. B **89**, 155433 (2014).

[15] B. Chen, H. Sahin, A. Suslu, L. Ding, M. I. Bertoni, F. M. Peeters, and S. Tongay, ACS Nano **9** (5), 5326 (2015).

[16] S. Cahangirov, M. Topsakal, E. Akturk, H. Sahin, and S. Ciraci, Phys. Rev. Lett. **102**, 236804 (2009).

[17] A. Kara, H. Enriquez, A. P. Seitsonen, L. C. L. Y. Voon, S. Vizzini, B. Aufray, and H. Oughaddou, Surf. Science Report. **67**, 1 (2012).

[18] V. Kochat, A Samanta, Y. Zhang, S. Bhowmick, P. Manimunda, S. Asif, A. S. Stender, R. Vajtai, A. K. Singh, C. S. Tiwary, and P. M. Ajayan, Sci. Adv. **4**, e1701373 (2018).

[19] S. V. Badalov, M. Yagmurcukardes, F. M. Peeters, and H. Sahin, J. Phys. Chem. C **122**, 28302 (2018).

[20] M. Nakhaee, M. Yagmurcukardes, S. A. Ketabi, and F. M. Peeters, Phys. Chem. Chem. Phys. **21**, 15798 (2019).

[21] A. P. Balan, S. Radhakrishnan, C. F. Woellner, S. K. Sinha, L. Deng, C. de los Reyes, B. M. Rao, M. Paulose, R. Neupane, A. Apte, V. Kochat, R. Vajtai, A. R. Harutyunyan, C.-Wu Chu, G. Costin, D. S. Galvao, A. A. Marti, P. A. van Aken, O. K. Varghese, C. S. Tiwary, A. M. M. R. Iyer, and P. M. Ajayan, Nat. Nanotech. **13**, 602 (2018).

[22] E. Kan, M. Li, S. Hu, C. Xiao, H. Xiang, and K. Deng, J. Phys. Chem. Lett. **4**, 1120 (2013).

[23] M. Marelli, A. Naldoni, A. Minguzzi, M. Allieta, T. Virgili, G. Scavia, S. Recchia, R. Psaro, and V. Dal Santo, ACS Appl. Mater. Interfaces **6**, 11997 (2014).

[24] M. Mishra and D.-M. Chun, Appl. Catal. A **6**, 126 (2015).

[25] J. Chen, L. Xu, W. Li, and X. Gou, Adv. Mater. **17**, 582 (2005).

[26] H. Zeng, J. Li, J. P. Liu, and Z. L. Wang, Nature **420**, 395 (2002).

[27] J. Katz, S. C. Riha, N. C. Jeong, A. B. F. Martinson, K. Omar, O. K. Farha, and J. T. Hupp, Coord. Chem. Rev. **256**, 2521 (2012).

[28] F. J. Morin, Phys. Rev. **78**, 819 (1950).

[29] T. Moriya, Phys. Rev. **120**, 91 (1960).

[30] R. D. L. Smith, M. S. Prevot, R. D. Fagan, Z. Zhang, P. A. Sedach, M. K. J. Siu, S. Trudel, and C. P. Berlinguette, Science **340**, 60 (2013).

[31] S. Sakurai, J.-I. Shimoyama, K. Hashimoto, and S. I. Ohkoshi, Chem. Phys. Lett. **458**, 333 (2008).

[32] A. Namai, M. Yoshikiyo, K. Yamada, S. Sakurai, T. Goto, T. Yoshida, T. Miyazaki, M. Nakajima, T. Suemoto, H. Tokoro, and S. I. Ohkoshi, Nat. Commun. **3**, 1035 (2012).

[33] S. I. Ohkoshi, S. Kuroki, S. Sakurai, K. Matsumoto, K. Sato, and S. Sasaki, Angew. Chem., Int. Ed. **46**, 8392 (2007).

[34] A. Namai, S. Sakurai, M. Nakajima, T. Suemoto, K. Matsumoto, M. Goto, S. Sasaki, and S. I. J. Ohkoshi, Am. Chem. Soc. **131**, 1170 (2009).

[35] N. V. Long, Y. Yang, M. Yuasa, C. M. Thi, Y. Q. Cao, T. Nann,and M. Nogami, RSC Advances **15**, 6383 (2014).

[36] X. L. Wu, Y. G. Guo, L. J. Wan, and C. W. Hu, J. Phys. Chem. C **112**, 16824 (2008).

[37] A. Banerjee, V. Aravindan, S. Bhatnagar, D. Mhamane, S. Madhavi, and S. Ogale, Nano Energy **2** (5), 890 (2013).

[38] X. Gu, L. Chen, Z. C. Ju, H. Y. Xu, J. Yang, and Y. T. Qian, Adv. Funct. Mater. **23**, 4049 (2013).

[39] W. S. Tang, Y. Su, Q. Li, S. A. Gao, and J. K. Shang, Water Res. **47**, 3624 (2013).

[40] C. Y. Cao, J. Qu, W. S. Yan, J. F. Zhu, Z. Y. Wu, and W. G. Song, Langmuir **28**, 4573 (2012).

[41] J. X. Wang, R. S. Yuan, L. Y. Xie, Q. F. Tian, S. Y. Zhu, Y. H. Hu, P. Liu, X. C. Shi, and D. H. Wang, RSC Advances **2**, 1112 (2012).

[42] G. H. Qiu, H. Huang, H. Genuino, N. Opembe, L. Stafford, S. Dharmarathna, and S. L. Suib, J. Phys. Chem. C **115**, 19626 (2011).

[43] J. L. Dormann, D. Fiorani, and E. Tronc, Adv. Chem. Phys. **98**, 283 (1997).

[44] R. D. Zysler, D. Fiorani, A. M. Testa, M. Godinho, E. Agostinelli, and L. Suber, J. Magn. Magn. Mater. **272**, 1575 (2004).

[45] D. Schroeer and R. C. Nininger, Phys. Rev. Lett. **19**, 632 (1967).

[46] M. Sorescu, R. A. Brand, D. Mihaila-Tarabasanu, and L. Diamandescu, J. Appl. Phys. **85**, 5546 (1999).

[47] R. I. Gonzalez, J. Mella, P. Díaz, S. Allende, E. E. Vogel, C. Cardenas, and F. Munoz, 2D Mater. **6** 045002 (2019).

[48] A. C. M. Padilha, M. Soares, E. R. Leite, and A. Fazzio, J. Phys. Chem. C **123**, 16359 (2019).

[49] B. Huang, G. Clark, E. Navarro-Moratalla, D. R. Klein, R. Cheng, K. L. Seyler, D. Zhong, E. Schmidgall, M. A. McGuire, D. H. Cobden, W. Yao, D. Xiao, P. Jarillo-Herrero, and X. Xu, Nature **546**, 270 (2017).

[50] G. Kresse and J. Hafner, Phys. Rev. B **47**, 558 (1993).

[51] G. Kresse and J. Furthmuller, Phys. Rev. B **54**, 11169 (1996).

[52] J. P. Perdew, K. Burke, and M. Ernzerhof, Phys. Rev. Lett. **77**, 3865 (1996).

[53] S. J. Grimme, J. Comput. Chem. **27**, 1787 (2006).

[54] S. L. Dudarev, G. A. Botton, S. Y. Savrasov, C. J. Humphreys and A. P. Sutton, Phys. Rev. B **57**, 1505 (1998).

[55] G. Henkelmana, A. Arnaldssonb, H. Jónsson, Comput. Mater. Sci. **36**, 354 (2006).

[56] D. Alfe, Comput. Phys. Commun. **180**, 2622 (2009).

[57] A. Fonari and S. Stauffer, "https://github.com/raman-sc/VASP/" (2013).

[58] M. Yagmurcukardes, C. Bacaksiz, E. Unsal, B. Akbali, R. T. Senger, and H. Sahin, Phys. Rev. B **97**, 115427 (2018).

[59] M. Yagmurcukardes, F. M. Peeters, and H. Sahin, Phys. Rev. B **98**, 085431 (2018).

[60] H. J. Xiang, E. J. Kan, S.-H. Wei, M.-H. Whangbo, and X. G. Gong, Phys. Rev. B **84**, 224429 (2011).

[61] D. Hayes, R. G. Hadt, J. D. Emery, A. A. Cordones, A. B. F. Martinson, M. L. Shelby, K. A. Fransted, P. D. Dahlberg, J. Hong, X. Zhang, Q. Kong, R. W. Schoenleinc, and L. X. Chen, Ener. Env. Sci. **9**, 3754 (2016).

[62] It should be noted that since Balan *et al.*[21] synthesized samples by exfoliation in crystalline directions of [001] and [010], there is a possibility that their Raman spectrum has also contribution from few-layers of [010] phase, but we do not expect significant differences in Raman activity of few-layer [001] and [010] hematite.

[63] It should also be noted that in calculation of electronic properties of a real semiconductor, independently from the smearing parameter, the bands are fully occupied and Fermi level is always in the band gap.